6-12-2012

Observed Seasonal Variations in Exospheric Effective Temperatures

E. J. Mierkiewicz
University of Wisconsin - Madison, mierkiee@erau.edu

F. L. Roesler
University of Wisconsin - Madison

S. M. Nossal
University of Wisconsin - Madison

Scholarly Commons Citation

Mierkiewicz, E. J., Roesler, F. L., & Nossal, S. M. (2012). Observed Seasonal Variations in Exospheric Effective Temperatures. *Journal of Geophysical Research, 117*(A06313). https://doi.org/10.1029/2011JA017123

Observed seasonal variations in exospheric effective temperatures

E. J. Mierkiewicz,[1] F. L. Roesler,[1] and S. M. Nossal[1]

Received 2 September 2011; revised 6 April 2012; accepted 30 April 2012; published 15 June 2012.

[1] High spectral resolution line profile observations indicate a reproducible semi-annual variation in the geocoronal hydrogen Balmer α effective temperature. These observations were made between 08 January 2000 and 21 November 2001 from Pine Bluff Observatory (WI) with a second generation double etalon Fabry-Perot annular summing spectrometer operating at a resolving power of 80,000. This data set spans sixty-four nights of observations (1404 spectra in total) over 20 dark-moon periods. A two cluster Gaussian model fitting procedure is used to determine Doppler line widths, accounting for fine structure contributions to the line, including those due to cascade; cascade contributions at Balmer α are found to be $5 \pm 3\%$. An observed decrease in effective temperature with increasing shadow altitude is found to be a persistent feature for every night in which a wide range of shadow altitudes were sampled. A semiannual variation is observed in the column exospheric effective temperature with maxima near day numbers 100 and 300 and minima near day numbers 1 and 200. Temperatures ranged from $\sim$710 to 975 K. Average MSIS model exobase temperatures for similar conditions are approximately 1.5$\times$ higher than those derived from the Balmer α observations, a difference likely due to contributions to the observed Balmer α column emission from higher, cooler regions of the exosphere.

Citation: Mierkiewicz, E. J., F. L. Roesler, and S. M. Nossal (2012), Observed seasonal variations in exospheric effective temperatures, *J. Geophys. Res.*, *117*, A06313, doi:10.1029/2011JA017123.

1. Introduction

[2] Ground-based Fabry-Perot observations of geocoronal hydrogen Balmer α nightglow (6563 Å) have become one of the primary methods to study the distribution of neutral atomic hydrogen in the upper thermosphere and exosphere [e.g., *Reynolds et al.*, 1973; *Atreya et al.*, 1975; *Meriwether et al.*, 1980; *Yelle and Roesler*, 1985; *Shih et al.*, 1985; *Kerr et al.*, 1986, 2001a, 2001b; *Kerr and Hecht*, 1996; *Kerr and Tepley*, 1988; *He et al.*, 1993; *Nossal et al.*, 1993, 1997, 1998, 2001, 2004, 2008; *Bishop et al.*, 2001, 2004; *Mierkiewicz et al.*, 2006]. Areas of focus include (1) high resolution observations of the geocoronal hydrogen Balmer α line profile and its relation to excitation mechanisms, effective temperature, and exospheric physics [*Atreya et al.*, 1975; *Meriwether et al.*, 1980; *Yelle and Roesler*, 1985; *Kerr et al.*, 1986; *Kerr and Hecht*, 1996; *Nossal et al.*, 1997, 1998]; (2) retrieval of geocoronal hydrogen parameters such as the hydrogen column abundance [H], the hydrogen density profile H(z), and the photochemically initiated hydrogen flux ϕ(H) [e.g., *Bishop et al.*, 2004; *He et al.*, 1993; *Kerr and Tepley*, 1988]; and (3) long term observations of the geocoronal hydrogen column emission intensity for the investigation of natural variability, such as solar cycle trends, and of potential anthropogenic change due to increases in atmospheric concentrations of greenhouse gases, especially CH_4 [e.g., *Nossal et al.*, 2008; *Kerr et al.*, 2001a]. Topic (1) is the main focus of this paper.

[3] Although ground-based observations of geocoronal hydrogen have been made over the last several decades with increasing instrumental capabilities, the technique of Fabry-Perot annular summing spectroscopy [*Coakley et al.*, 1996] has enabled a tremendous leap forward in both the achieved signal-to-noise and temporal resolution of geocoronal Balmer α data sets. Early applications of the annular summing technique [*Nossal et al.*, 1997, 1998], however, were retrofits to traditional scanning Fabry-Perot spectrometers, and suffered from instrumental vignetting that compromised the full advantage of the annular summing technique.

[4] The data presented in this paper are the first geocoronal line profile observations obtained with a Fabry-Perot employing an optical system specifically designed for the annular summing technique [*Mierkiewicz et al.*, 2006]. The net result is an instrument capable of making geocoronal observations with a signal-to-noise ratio of $\sim$100 in 10 min, covering a nearly unvignetted 75 km/s spectral interval with 3.75 km/s velocity resolution.

[5] The structure of this paper is as follows. In section 2 we briefly review past Balmer α line profile observations. In sections 3 and 4 we review important concepts regarding geocoronal Balmer α excitation and effective temperature. Our observing strategy, signal-to-nose estimates, and data

[1]Department of Physics, University of Wisconsin-Madison, Madison, Wisconsin, USA.

Corresponding author: E. J. Mierkiewicz, Department of Physics, University of Wisconsin-Madison, Madison, WI 53706, USA. (emierk@astro.wisc.edu)

reduction procedures are discussed at length in sections 5–7. Because the accurate interpretation of geocoronal line profiles in terms of an effective temperature depends so heavily on excitation mechanisms (i.e., cascade) and the Galactic Balmer α background emission, sections 3–7 build a foundation for the results presented in this paper. These results, primarily focusing on geocoronal effective temperatures and their variations with altitude and season, are presented in section 8; we discuss these results in section 9.

2. A Brief Review of Balmer α Line Profile Observations

[6] *Atreya et al.* [1975] first demonstrated the feasibility of using a (single-etalon) Fabry-Perot spectrometer to observe geocoronal Balmer α line profiles at high spectral resolution ($R \sim 100{,}000$). A Fourier analysis technique [*Hays and Roble*, 1971] was used to filter and analyze the data; observations obtained each night were added together (via their Fourier coefficients) in order to boost the low signal-to-noise (S/N) data.

[7] Observed distortions in the wings of the line were attributed to spectral contamination from three nearby hydroxyl lines of the OH(6–1) band, lying approximately +6.2, +10.7, and −9.1 Å from the Balmer α emission [*Atreya et al.*, 1975]. Once corrected for OH contamination, nightly mean temperatures (2 nights in December 1971, 3 nights in May 1972, and 1 night in October 1972) were found to be between 700–850 K, temperatures 50–200 K lower than the empirical temperature model of *Jacchia* [1971].

[8] *Meriwether et al.* [1980] modified the Fabry-Perot used by *Atreya et al.* [1975] and gained a factor of 25 in sensitivity (the resolving power remained ∼100,000). This gain resulted in a significant increase in temporal resolution, with an effective temperature determined in approximately one hour. *Meriwether et al.* [1980] observed Balmer α line profiles with this modified system from Arecibo Observatory (Puerto Rico) on March 12/13 and 14/15, 1980. A significant decrease in effective temperature was observed in the March 14/15 data set, decreasing from ∼1200–1400 K in the early evening, to ∼400 K near local midnight; shadow altitude increased from ∼500 km to nearly 20,000 km during this interval.

[9] *Meriwether et al.* [1980] found their data to be consistent with an observed decrease in Lyman α thermal width with distance from the earth, detected via hydrogen absorption cell measurements onboard the *OGO–5* satellite [*Bertaux and Blamont*, 1970; *Bertaux*, 1978]. The data also appeared consistent with the absence of a downward moving population of atoms at high shadow altitudes, whose velocities exceed the escape velocity (i.e., a blue-wing line profile depletion due to escape) [*Meriwether et al.*, 1980]. The authors pointed out that any quantitative comparison with theory would require an assessment of the magnitude of radiative transport of Lyman β into the earth's shadow (i.e., multiple-scattering), work later carried out by *Anderson et al.* [1987].

[10] Subsequent Balmer α line profile and intensity observations were made at Arecibo by *Kerr et al.* [1986, 2001a, 2001b], *Kerr and Tepley* [1988], and *He et al.* [1993] using a Fabry-Perot similar in design to that of *Meriwether et al.* [1980]. *Kerr et al.* [1986] also reported a decrease in thermal width with shadow altitude.

[11] Line profile observations were also conducted by Wisconsin observers beginning with *Yelle and Roesler* [1985], from Madison, WI, in October 1983 and March 1984. *Yelle and Roesler* [1985] used a double etalon Fabry-Perot ($R \sim 110{,}000$), in which two etalons are combined in series. This configuration enables high spectral purity and contrast by extending the free spectral range (i.e., the spectral distance between adjacent orders of transmission) and suppressing the broad Lorentzian wings of a single etalon transmission function [*Roesler*, 1974]. The second etalon also sharpens the common transmission peak of the two etalon system [*Daehler and Roesler*, 1968]. The etalons used by *Yelle and Roesler* [1985] employed a vernier spacer ratio combination in order to eliminate contamination of the Balmer α signal from the nearby lines of the OH(6–1) band.

[12] *Yelle and Roesler* [1985] observed a narrowing of the Balmer α profile with shadow altitude, consistent with the earlier observations of *Meriwether et al.* [1980]; profiles appeared essentially Gaussian at low shadow altitudes, but became markedly non-Gaussian at high altitudes, with a sharp decrease in line width near local midnight. A number of anomalous profiles (i.e., slightly blue shifted and box-shaped) were also observed at high shadow altitudes (i.e., near local midnight), seemingly connected to moderately high geomagnetic activity (Ap ∼ 35). A red-wing asymmetry was also detected, which appeared to be consistent with an enhanced escape flux due to charge-exchange or the presence of Balmer α fine structure components not present in direct solar Lyman β fluorescent scattering.

[13] Employing a single scattering Lyman β excitation model, using an algorithm similar to that described by *Bertaux* [1978], *Yelle and Roesler* [1985] concluded that their observed Balmer α thermal widths, and those of *Meriwether et al.* [1980], were approximately a factor of two cooler than predicted from theory [*Chamberlain*, 1963, 1976]. *Yelle and Roesler* [1985] speculated that the narrowing of their observed profiles with altitude may be related to satellite atom populations in which atoms with large apogees (or large eccentricities) were depleted, or perhaps the result of Lyman β radiative transport into the earth's shadow illuminating cooler hydrogen in the lower thermosphere, or some combination of the two. Work by *Anderson et al.* [1987] would later demonstrate that the multiple scattering component can in fact be a large fraction of the total observed column emission, depending on viewing geometry.

[14] The Fabry-Perot spectrometers employed by *Atreya et al.* [1975], *Meriwether et al.* [1980], *Kerr et al.* [1986, 2001a, 2001b], *Kerr and Tepley* [1988], *He et al.* [1993] and *Yelle and Roesler* [1985] all used single-channel photomultiplier (PMT) detection techniques in which single resolution elements of the Fabry-Perot's annular interference pattern are sequentially sampled, thereby constructing a spectrum by scanning over the desired spectral interval [see, e.g., *Roesler*, 1974]. Application of the charge-coupled-device (CCD) to Fabry-Perot spectroscopy in the 1990s via the annular summing technique [see *Coakley et al.*, 1996] greatly improved the quality and quantity of ground-based upper atmospheric emissions data.

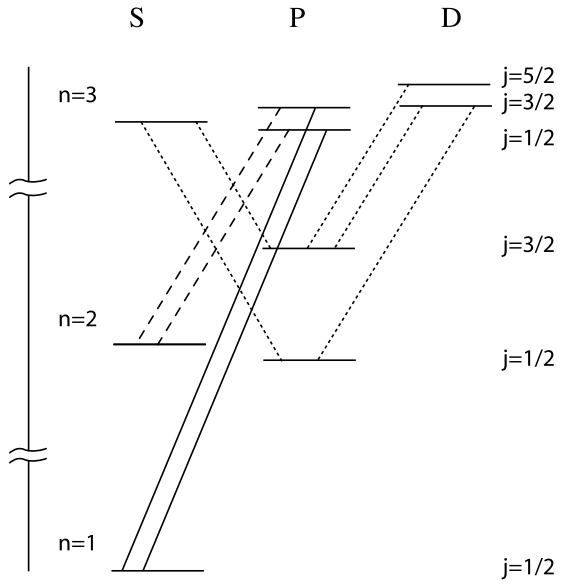

Figure 1. Atomic hydrogen energy level diagram showing the seven allowed Balmer α ($3 \rightarrow 2$) transitions (dotted and dashed lines). In the case of direct solar Lyman β excitation (solid lines) only the $3^2P_{1/2,3/2}$ levels are populated, resulting in emission from only two fine structure components ($3P_{3/2} \rightarrow 2S_{1/2}$ and $3P_{1/2} \rightarrow 2S_{1/2}$) indicated by dashed lines.

[15] Using a CCD/annular-summing system, *Nossal et al.* [1997, 1998] demonstrated that it was possible to obtain Balmer α data with sufficient *S*/*N* for detailed line profile studies with integration times as short as 4–15 min. These observations enabled a more accurate study of the Balmer α line shape, which led to the conclusion that the Balmer α red-wing asymmetries observed by *Yelle and Roesler* [1985] were consistent with additional fine structure components via cascade.

[16] *Nossal et al.* [1998] observed a $\sim$10% cascade enhancement, slightly higher than predictions by *Meier* [1995] that $\sim$7% of the total Balmer α intensity is due to cascade emission. *Nossal et al.* [1997] also determined that exospheric temperatures determined from fits to Balmer α profiles which neglect cascade contributions are on average 130 K higher than those determined using a fit accounting for all cascade components. The CCD/annular-summing observations of *Nossal et al.* [1997] suggested the possibility of seasonal influences on the emission profile, but the authors concluded that further observations were needed for confirmation.

[17] The new observations presented in this paper build on the demonstration observations of *Nossal et al.* [1997, 1998]. The Fabry-Perot optics were designed to optimize the spectrometer for the annular summing technique, thereby reducing vignetting, improving the background characterization and extending the spectral range [*Mierkiewicz et al.*, 2006]. This second generation Fabry-Perot annular summing spectrometer enabled the acquisition of a comprehensive monthly data set spanning 20 dark moon periods during 2000–2001. As presented in section 8, this resulted in the detection of a reproducible semiannual variation in the observed exospheric effective temperatures near the exobase, with maxima near day numbers 100 and 300 and minima near day numbers 1 and 200.

3. Excitation and Emission

[18] The Balmer α ($n = 3 \rightarrow 2$) transition of atomic hydrogen is composed of seven possible fine structure components. Refer to Figure 1 and Table 1. The relative population rates of the 3S, 3P and 3D parent terms depend on the excitation mechanism. The intensity ratios for lines within a multiplet (e.g., the $3P \rightarrow 2S$ doublet) follow quantum mechanics [see, e.g., *Bethe and Salpeter*, 1957]; referring to the component numbers in Table 1, I_2:I_4 = 2:1, I_3:I_7 = 1:2, and I_6:I_5: I_1 = 1:9:5.

[19] Geocoronal hydrogen Balmer α fluorescence arises primarily from solar Lyman β (1025.72 Å) excitation. The only allowed Lyman β transitions populate the $3P_{1/2,3/2}$ levels as shown in Figure 1. These levels decay 88% of the time to the ground state and 12% of the time to $2S_{1/2}$, the latter transition resulting in Balmer α. Thus, Balmer α emission by direct solar Lyman β excitation is a blend of two fine structure components ($3P_{3/2} \rightarrow 2S_{1/2}$ and $3P_{1/2} \rightarrow 2S_{1/2}$) in a 2:1 intensity ratio, with a vacuum wave number line center of gravity of 15233.3280417 cm^{-1} (λ_{air} = 6562.74 Å) [*Garcia and Mack*, 1965].

3.1. Cascade

[20] Geocoronal hydrogen atoms are also excited by solar Lyman lines beyond Lyman β to energy states $n > 3$, some of which cascade to $n = 3$, populating levels (3*S* and 3*D*) not allowed by direct Lyman β excitation alone. When these levels decay to $n = 2$, they add emission line components

Table 1. Balmer α Emission Components and *g*–Factors

Component	Transition	σ[a] (cm^{-1})	λ_{air}[b] (Å)	Δv[c] (km s^{-1})	*g* Direct[d] (s^{-1})	*g* Cascade[d] (s^{-1})
1	$3^2D_{3/2} \rightarrow 2^2P_{1/2}$	15233.399279	6562.710	−2.824	0	9.34×10^{-10}
2	$3^2P_{3/2} \rightarrow 2^2S_{1/2}$	15233.364177	6562.725	−2.133	2.64×10^{-7}	2.29×10^{-10}
3	$3^2S_{1/2} \rightarrow 2^2P_{1/2}$	15233.301551	6562.752	−0.90	0	9.00×10^{-9}
4	$3^2P_{1/2} \rightarrow 2^2S_{1/2}$	15233.255771	6562.772	0.0	1.32×10^{-7}	1.15×10^{-10}
5	$3^2D_{5/2} \rightarrow 2^2P_{3/2}$	15233.06954	6562.852	3.665	0	1.68×10^{-9}
6	$3^2D_{3/2} \rightarrow 2^2P_{3/2}$	15233.033406	6562.868	4.376	0	1.86×10^{-10}
7	$3^2S_{1/2} \rightarrow 2^2P_{3/2}$	15232.935678	6562.910	6.299	0	1.80×10^{-8}

[a]Vacuum wave numbers from *Garcia and Mack* [1965].
[b]$\lambda_{air} = \lambda_{vac}/\mu$, where μ = 1.0002762 at Balmer α.
[c]Velocity intervals are referenced to component 4.
[d]*g*-factors (direct and cascade) from *Meier* [1995]; in the absence of large Doppler shifts, or complications due to multiple scattering or extinction, the ratios of the emission *g*-factors are equal to the ratios of the line intensities.

from all seven possible Balmer α transitions (refer to Figure 1). In this way cascade from higher levels alters the observed geocoronal Balmer α line profile by adding emission along fine structure paths not present in direct solar Lyman β excitation [*Yelle and Roesler*, 1985; *Chamberlain*, 1987; *Meier*, 1995; *Nossal et al.*, 1998].

[21] A detailed knowledge of solar Lyman line shapes is necessary to calculate geocoronal hydrogen excitation and emission rates (g-factors). Using the high spectral resolution solar observations of *Tousey et al.* [1965] (Lyman α through κ), combined with the absolute fluxes of *Hinteregger et al.* [1981] and a pseudocontinuum for Lyman 10 through the Lyman continuum (based on the observations of *Vernazza and Reeves* [1978]), *Meier* [1995] evaluated the effect of cascade on the Balmer α emission, calculating excitation rates of the 3*S*, 3*P* and 3*D* parent terms of the Balmer α multiplet.

[22] *Meier*'s [1995] Balmer α emission *g*-factors, partitioned among all seven fine structure components, for both direct and cascade induced emission, are given in Table 1. The 3*S* transitions, where the 3*S* parent term is predominately populated by cascade from solar Lyman γ excitation, are favored over the other Balmer α cascade contributions by an order of magnitude.

[23] *Meier* [1995] estimated that approximately 7% of the total Balmer α emission (near solar minimum conditions) is in the form of cascade. Revised calculations based on more recent high-resolution disk averaged solar line profiles (also near solar minimum) [*Warren et al.*, 1998] adjusts *Meier*'s [1995] cascade numbers somewhat lower, to ~4% at Balmer α (R. R. Meier, private communication, 2000).

3.2. LOS Shadow Altitude

[24] In addition to solar Lyman line center flux, observed geocoronal Balmer α column emission rates also depend on the atomic hydrogen altitude profile and viewing geometry. Typical nighttime zenith Balmer α intensities range from ~15 Rayleighs for observations near the terminator to ~2 R near local midnight (1 R = $10^6/4\pi$ photons s^{-1} cm^{-2} sr^{-1}). The observed variation in the Balmer α emission is strongest with respect to solar depression angle (SDA) and the related quantity line-of-sight (LOS) shadow altitude.

[25] LOS shadow altitude is defined as the altitude of the point where a nightside ground-based observer's line-of-sight exits the planetary shadow cylinder defined by the resonant radiation "black level" altitude at the terminator: 102 km for Lyman β, due to O_2 screening. For useful diagrams depicting LOS shadow altitude, see, e.g., *He et al.* [1993], *Shih et al.* [1985] and *Anderson et al.* [1987]. Atomic hydrogen column densities above 100 km are large enough, however, that multiple scattering of Lyman β into the Earth's shadow will contribute to the observed Balmer α column emission, becoming an increasing fraction of the total emission as the LOS shadow altitude increases [*Anderson et al.*, 1987; *Bishop et al.*, 2001].

4. Effective Temperature

[26] A thermal population of emitting atoms will have a Gaussian line shape centered at the rest wavelength $\lambda_\circ$ of the emission (assuming no bulk motion), with a line width $\Delta\lambda_{fwhm}$ proportional to the square root of the temperature T of the emitting population,

$$\Delta\lambda_{fwhm} = 2\lambda_\circ \sqrt{\frac{2kT\ln(2)}{mc^2}}. \quad (1)$$

For atomic hydrogen, equation (1) becomes,

$$\Delta\lambda_{fwhm} = 7.14 \times 10^{-7} \lambda_\circ \sqrt{T} \quad (2)$$

where T is in units of kelvin (K).

[27] A high frequency of collisions preserves a Maxwellian velocity distribution near the exobase and line profiles dominated by Doppler broadening (equations (1) and (2)). Above this critical layer, thermal equilibrium breaks down and the emission line profiles are no longer truly Gaussian [see, e.g., *Bishop and Chamberlain*, 1987]. As such, in the exosphere T in equation (2) will be considered an *effective temperature* (T_{eff}), where

$$T_{eff} = 1.96 \times 10^{12} \left(\frac{\Delta\lambda_{fwhm}}{\lambda_\circ}\right)^2 [\mathrm{K}]. \quad (3)$$

A spectral scale in units of velocity $v = c(\Delta\lambda/\lambda_\circ)$ [km/s] will be used almost exclusively in this paper due to its utility in determining spectral shifts between terrestrial and Galactic sources of emission and its facility in the interpretation of geocoronal observations. A spectral interval of 1 km/s corresponds to 0.0219 Å at Balmer α.

5. The 2000–2001 Observations

[28] Velocity-resolved geocoronal Balmer α line profile observations were carried out with a large aperture (15 cm), double etalon, second generation Fabry-Perot CCD/annular-summing spectrometer located at the Pine Bluff Observatory (PBO) near Madison, WI (43.07°N, 270.33°E). The PBO Fabry-Perot is coupled to a siderostat with a circular ~1.5° field-of-view on the sky, sampling a 75 km/s spectral interval (~1.6 Å) with 3.75 km s^{-1} (~0.08 Å at Balmer α) spectral resolution ($R = \lambda/\Delta\lambda \approx 80{,}000$). The central wavelength of the 75 km/s spectral window is selected by pressure tuning using a N_2 gas system. A narrow band (~20 Å) interference filter provides additional spectral isolation. See *Mierkiewicz et al.* [2006] for further details.

[29] The annular summing technique involves imaging the Fabry-Perot annular fringe pattern onto a low noise, cryogenically cooled charge-coupled device (CCD) with high quantum efficiency (~80% at Balmer α); refer to Figure 2a. The CCD used for these observations was a Photometrics model CH360, with a 512 × 512 array of 24 μm pixels binned 2 × 2. The camera was operated at a gain of 1.22 e^-/ADU with a read noise of 10 e^-/pixel. The PBO CCD was cooled to approximately −110°C, resulting in a dark contribution of <0.001 e^-/pixel/s.

[30] In order to mitigate spectral contamination from solar features (in particular a deep solar Fraunhofer absorption line at Balmer α) observations were limited to nighttime periods with solar depression angles ≥10 deg when the moon was also below the horizon. All observations were conducted on clear nights during a two-week period centered on new moon.

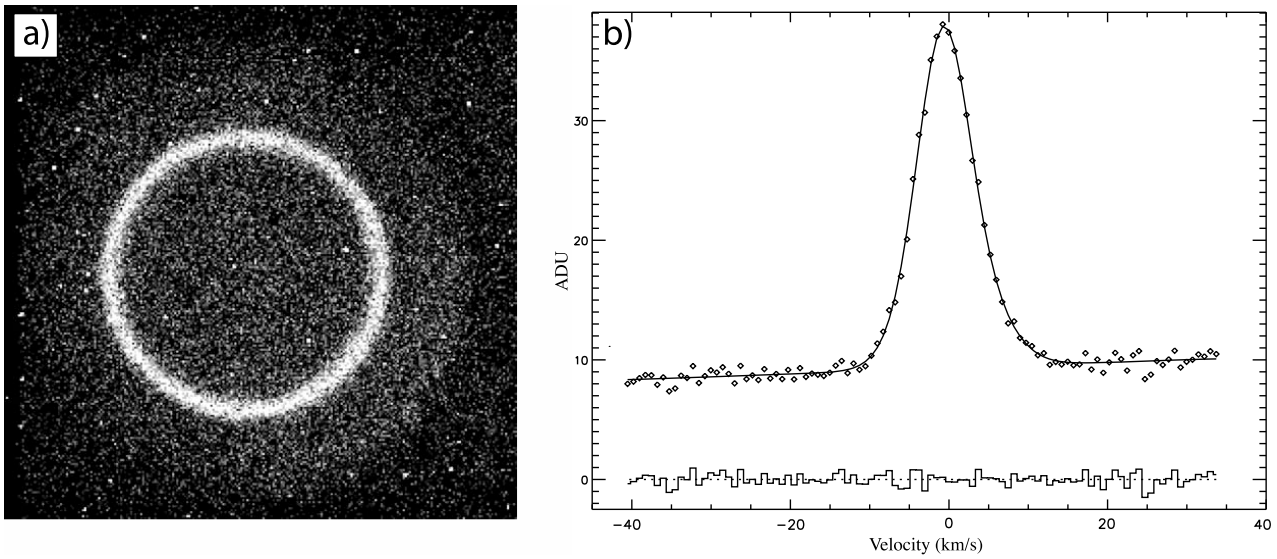

Figure 2. (a) An example Balmer α fringe imaged onto the PBO CCD (512 × 512 array of 24 μm pixels binned 2 × 2) in a 600 s integration. The radial position of the fringe is selected such that there is nearly equal spectral baseline to the red (toward the center of the fringe) and to the blue (toward the edge of the CCD). Using the property that equal area annuli in the Fabry-Perot interference pattern correspond to equal spectral intervals, Figure 2a is divided into equal area annular elements; the radius of the central resolution element is 22 binned pixels, corresponding to a spectral interval of 3.75 km/s. Twenty resolution elements were imaged onto the CCD (i.e., 75 km/s). (b) The resulting line profile (5× over sampling with 0.75 km/s per sample element). A two cluster Gaussian fit to the data is indicated in Figure 2b by a solid line; residuals (i.e., the difference between the data and fit) are also included.

[31] Coupling of the PBO Fabry-Perot to a siderostat allowed observations to be made over a wide range of viewing geometries while also avoiding regions of significant Galactic Balmer α emission [see, e.g., *Haffner et al.*, 2003]. All observations were obtained at least 10 degrees away from the Galactic plane.

[32] The orbital velocity of the earth and the peculiar velocity of the sun (v = 20.0 km/s toward $\alpha(1900) = 18.0^h$, $\delta(1900)$ = +30.0 deg) with respect to the local standard of rest (LSR) introduce a velocity separation (VLSR) between the geocentric rest frame and zero LSR, the magnitude of which depends on look direction and time of year. As the majority of the local Galactic Balmer α emission occurs near 0 km/s LSR [*Haffner*, 1999], the Galactic component of emission in each geocoronal spectrum is usually located near VLSR. As such, observation directions were also selected in order to maximize VLSR. Such a scheme makes it easier to resolve the relatively broad (∼20 km/s *fwhm*) Galactic Balmer α emission from the narrow (∼7 km/s *fwhm*) geocoronal line, thereby reducing uncertainties in the interpretation of geocoronal line profiles due to Galactic contamination. Only spectra in which |VLSR| ≥ 10 km/s are included here. In some look directions non-local Galactic Balmer α, Doppler shifted from 0 km/s LSR by differential Galactic rotation, can also contaminate geocoronal observations. For this reason, velocity resolved maps of Galactic Balmer α [*Haffner et al.*, 2003] were consulted when planning these observations.

[33] All observations were obtained with right-ascension (α) and declination (δ) fixed (i.e., tracking at the sidereal rate). In this way the interstellar hydrogen background remained constant for each geocoronal spectrum. In order to explore the red-wing of the geocoronal emission profile for signatures of cascade emission, free of Galactic contamination, observation look directions in which the Galactic emission was Doppler shifted to the blue of the telluric line were favored. Finally, to limit the effects of scattering and absorption in the lower atmosphere and to simplify the interpretation of the line profiles, observations were also made as close to the zenith as possible given the aforementioned restrictions.

6. Signal-to-Noise Ratio

[34] The number of photons per second, N_{line}, above the background level hitting the detector in one resolution element ($\lambda/R_\circ$, where $R_\circ$ is the theoretical resolving power) is given by,

$$N_{line} = (0.8)\epsilon A\Omega \frac{I_{line} \times 10^6}{4\pi} \frac{\delta\lambda}{\Delta\lambda_{line}} \quad (4)$$

where 0.8 is the average transmitted intensity of the line within the full width at half maximum (*fwhm*), I_{line} is the integrated intensity of the source in Rayleighs, A is the area of the etalon plates (cm^2), $\Omega = (2\pi/R_\circ)$ is the solid angle subtended by a resolution element, ϵ is the efficiency of the optical system (including the quantum efficiency of the detector), and $\delta\lambda/\Delta\lambda_{line}$ is the inverse of the number of resolution elements $\delta\lambda$ in the observed line width (*fwhm*)

$\Delta\lambda_{line}$. The signal is then the product of the rate (N_{line}) and the integration time t.

[35] Noise terms include contributions from the sky background, CCD dark current, and read noise. The background count rate in one resolution element (N_{back}) is similar to that of N_{line}, but with the continuum background intensity I_{back} (R/Å) integrated over a resolution element (i.e., $I_{back}\delta\lambda$),

$$N_{back} = \epsilon A\Omega \frac{(I_{back}\delta\lambda) \times 10^6}{4\pi}. \quad (5)$$

[36] The signal-to-noise (S/N) ratio is then,

$$\left(\frac{S}{N}\right)_{est} = \frac{N_{line}t}{\sqrt{(N_{line} + N_{back} + N_{dark})t + R_n^2 p}} \quad (6)$$

where t is the total integration time, R_n the RMS read noise, p is the number of pixels in one resolution element, and N_{dark} is total dark current per resolution element (note, $N_{dark} = Dp$, where D is the dark current per pixel per second).

[37] The efficiency of the PBO optical system is estimated to be $\epsilon = 0.08$; the resolving power is $R = 80{,}000$ (3.75 km/s), the etalon diameter was typically stopped down to 10 cm. With a 3.75 km/s resolution element and a geocoronal line width of ~7 km/s, $\delta\lambda/\Delta\lambda_{line} = 0.5$. Assuming a geocoronal Balmer α emission line with $I_{line} = 5$ R (a typical intensity for a shadow altitude of 2500 km) in the presence of a 2 R/Å (0.16 Rayleigh per resolution element) background, by equations (4) and (5), $N_{line} = 79$ e$^-$/s and $N_{back} = 6$ e$^-$/s. With a measured dark current of $D = 0.001$ e$^-$/pixel/s and $p = 1520$ pixels, $N_{dark} = 1.52$ e$^-$/s. The read noise for the PBOCCD is $R_n = 10$ e$^-$/pixel. Based on these estimates, the PBO Fabry-Perot is read noise dominated; $N_{back} + N_{dark}$ do not contribute significantly to the total signal-to-noise ratio.

[38] Given the form of equation (6), the read noise term can be overcome if $N_{line} + N_{back}$ is large, or if the integration time is long enough to make the read noise term small in comparison to the integrated signal. An integration time of 600s was used to overcome the read noise limitations of the PBO CCD and achieve a signal-to-noise ratio near 100 required for detailed line profile analysis (i.e., from equation (6), $(S/N)_{est} \approx 100$ for a 600 s integration on a 5 R line). See *Coakley et al.* [1996] for additional details.

7. Data Reduction

[39] Processing of the PBO geocoronal Balmer α data set includes bias subtraction, filtering to remove cosmic rays, and annular summing.

[40] Making use of the property that equal area annuli in the Fabry-Perot interference pattern correspond to equal spectral intervals, the CCD image of the annular fringe pattern is divided into equal area annular elements, and reassembled, to provide a spectral profile [*Coakley et al.*, 1996]. The area of an annular sample element is selected to subdivide each nested resolution element into smaller spectral intervals, where a resolution element is defined by the full width at half maximum of the spectrometer's instrumental function. Refer to Figures 2a and 2b and *Mierkiewicz et al.* [2006] for further details.

[41] A flatfield correction has not been applied to this data set. In general, flatfield images are typically needed to correct for variations in sensitivity due to vignetting within the instrument, and to correct for pixel-to-pixel variations in the quantum efficiency of the CCD. As each annular element used in the PBO analysis contains ~300 pixels, pixel-to-pixel variations are averaged out; there is no evidence for any large scale structure on the chip beyond a small amount of fixed pattern noise which is removed during bias subtraction [*Mierkiewicz et al.*, 2006]. The redesigned optical system of the PBO Fabry-Perot by *Mierkiewicz* [2002] greatly reduced the magnitude of instrumental vignetting associated with the earlier CCD/annular-summing demonstration observations of *Nossal et al.* [1997]. The net result is a nearly unvignetted 75 km/s spectral range with an estimated 10% loss in efficiency from the red to the blue end of the 75 km/s spectral window [*Mierkiewicz et al.*, 2006].

7.1. Fits to the Data

[42] Individual spectra were reduced using a 4-parameter fit procedure incorporating nine Gaussian line components grouped into two clusters and convolved with an instrumental profile. The first cluster contains the two fine structure lines directly excited by Lyman β scattering with a fixed 2:1 emission ratio. The second cluster contains the full set of seven Balmer α fine structure components with the line ratios given in *Meier* [1995] and Table 1. The $3P_{3/2} \rightarrow 2S_{1/2}$ and $3P_{1/2} \rightarrow 2S_{1/2}$ transitions are included twice since these transitions include contributions from both direct excitation and cascade.

[43] The four free parameters in this fitting procedure are the total intensities of each of the two clusters, the line width (common to all fine structure components), and the spectral position of the emission feature. The spectral spacing between fine structure components is set by atomic physics; all fine structure components are referenced to the $3P_{1/2} \rightarrow 2S_{1/2}$ transition (refer to Table 1). Model fit parameters are iterated, subject to the above constraints, to produce a least squares, best-fit to the data using the Voigt-fit code of R. C. Woodward (private communication, 2011).

[44] The 6554 Å line of thorium (excited in a hollow cathode lamp) was used to obtain a measure of the instrument profile (IP), where it is assumed that all observed broadening to the thorium emission is due to instrumental effects. Thorium is a heavy, even-even nucleus atom, and therefore produces very narrow emission lines with no hyperfine structure. The predicted width of the thorium hollow cathode emission with a discharge temperature of ~1000 K is 0.42 km/s, approximately 1/10th the measured line width for the PBO Fabry-Perot at a resolving power of 80,000. Neglecting the inherent width of the thorium emission introduces a negligible −4 K systematic error in temperature when interpreting the Balmer α line profile in terms of an effective temperature [*Nossal et al.*, 1997]. Plate reflectivity and phase shifts in the etalon coatings are negligible over the short spectral interval between the 6554 Å and 6563 Å emission lines. In order to minimize uncertainties in the IP due to imperfections in the optical imaging of the ring pattern onto the CCD, the IP was observed at a ring radius close to that of the night-sky emission [*Coakley et al.*, 1996].

[45] In order to isolate the thorium 6554 Å emission line from other nearby features, the spectral range near the 6554

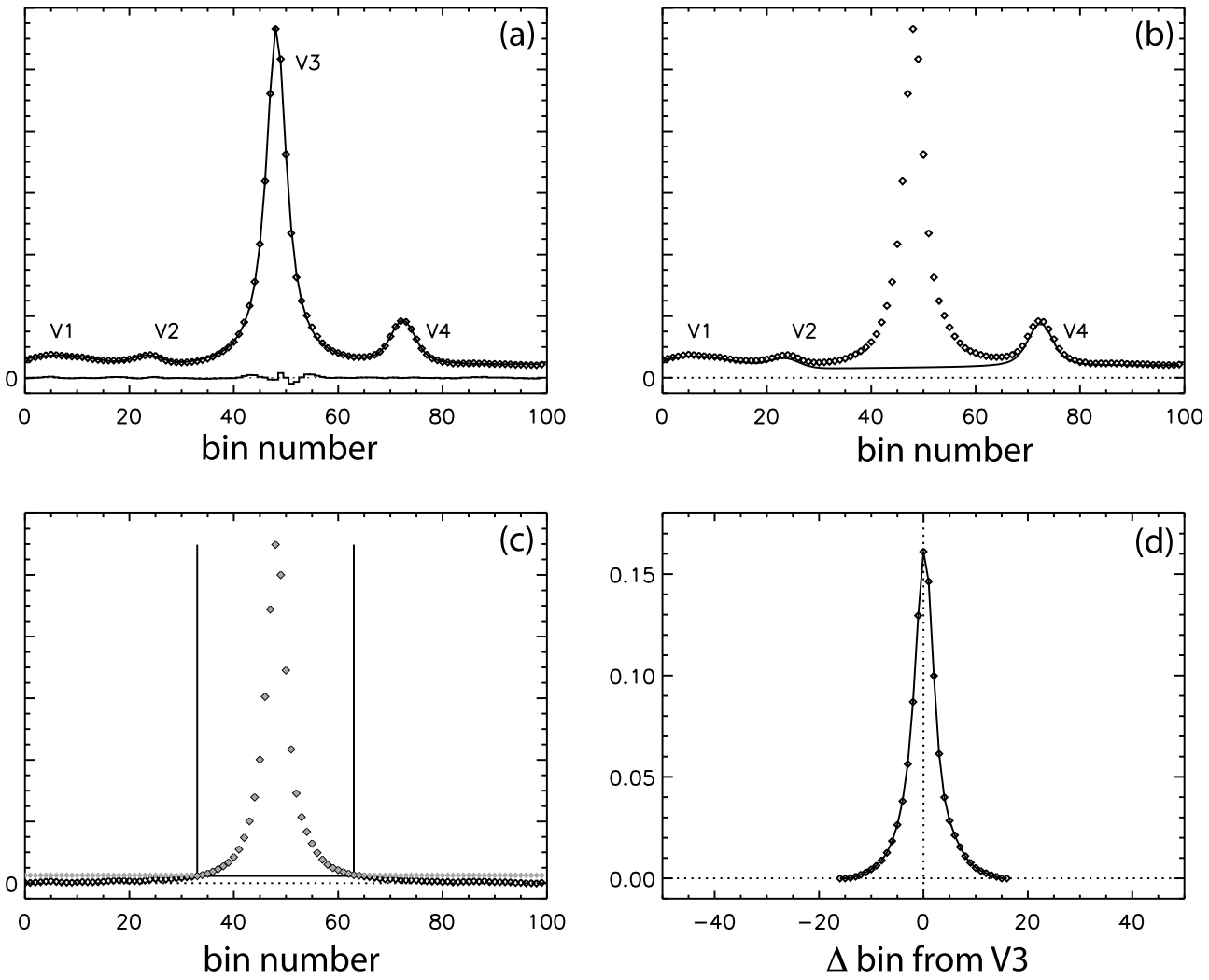

Figure 3. (a) The thorium 6554 Å line (bright line near bin 50) was used as the instrumental profile (IP) in the PBO analysis. The average measured *fwhm* of this emission was found to be 3.75 km/s, corresponding to a resolving power of 80,000. (a) The full 75 km/s range is fit with a four component model and a sloping background. (b) The three components corresponding to background features in the spectra are isolated, and (c) subtracted. (d) The IP itself is defined as the region ±15 bins from the center of component V3. On most nights the IP was measured several times; see Tables 2 and 3.

Å emission was fit with a four component model and a sloping background. Refer to Figure 3. Once fit, the three components corresponding to "background features" in the lamp were subtracted, thereby isolating the 6554 Å emission line (refer to Figures 3b and 3c). The PBO IP was defined as the region ±15 sample elements from the center of the fit component corresponding to the thorium 6554 Å emission line (Figure 3d), where one sample element is equal to 0.75 km/s [*Mierkiewicz et al.*, 2006]. The average measured *fwhm* of the thorium 6554 Å emission line was 3.75 ± 0.25 km/s (i.e., $R \approx 80{,}000$).

[46] The spectral dispersion across the CCD was calibrated using images of two pairs of well known thorium lines at: 6564.4443 Å, 6565.0698 Å, and 6560.0576 Å, 6558.8755 Å. The spectral intervals between these lines allowed the 0.75 km/s spectral interval per sample element of the PBO spectrometer to be determined [*Mierkiewicz et al.*, 2006]. The dispersion was assumed to be linear across the 75 km/s spectral window centered on Balmer α.

8. Results

[47] Sixty-four nights of high-resolution geocoronal Balmer α line profile observations (1404 spectra in total) were made from PBO over 20 dark moon periods between 08 January 2000 and 21 November 2001. This data set spans an interval near solar maximum, with solar/geophysical conditions fluctuating from moderate to high activity. Tables 2 and 3 list individual observation dates, corresponding Ap and F10.7 indices, and the number of spectra collected each night. Spectra taken during the same dark moon observing window are assigned a series number; data from twenty series are included in this paper corresponding to 20 dark moon periods; see Table 4.

Table 2. The 2000–2001 Balmer α Data Set: Nights 1–32

Night	Series	Date	Day[a]	Spc[b]	IP[c]	F10.7	Ap
1	1	01/08/00	08	22	0	150	05
2	1	01/09/00	09	3	0	155	03
3	1	01/14/00	14	7	0	195	08
4	2	01/27/00	27	9	0	128	17
5	2	01/28/00	28	19	0	122	32
6	2	02/02/00	33	23	2	140	08
7	2	02/05/00	36	37	1	163	12
8	2	02/08/00	39	20	1	169	15
9	3	02/28/00	59	7	2	215	16
10	3	03/02/00	62	35	6	210	11
11	3	03/03/00	63	40	7	200	05
12	3	03/04/00	64	30	8	197	03
13	3	03/05/00	65	44	8	217	06
14	3	03/06/00	66	42	9	219	12
15	4	03/30/00	90	30	7	205	12
16	4	04/05/00	96	37	9	195	11
17	4	04/06/00	97	22	10	178	82
18	5	04/30/00	121	25	6	172	12
19	5	05/02/00	123	19	6	155	21
20	5	05/03/00	124	12	5	140	17
21	6	06/06/00	158	26	5	192	15
22	6	06/09/00	161	18	4	174	05
23	7	08/25/00	238	8	3	136	03
24	7	08/28/00	241	14	2	163	27
25	7	09/05/00	249	26	5	183	07
26	7	09/06/00	250	21	5	182	12
27	8	09/26/00	270	29	9	225	24
28	8	09/27/00	271	14	8	206	11
29	8	09/28/00	272	12	7	203	12
30	8	09/29/00	273	23	7	193	07
31	8	10/03/00	277	16	6	192	30
32	9	10/19/00	293	11	3	157	09

[a]Day number; year 2000 was a leap year, as such 02/29/00 is day 60.
[b]Number of spectra with: shadow altitudes <20,000 km, observation zenith distances ≤45°, galactic latitudes >10° from the plain (l = 0).
[c]Number of instrumental profiles (IPs) collected per night.

[48] Because various slant paths (defined by the zenith and azimuth angles of the observation) can correspond to the same LOS shadow altitude, the data has been differentiated by observational zenith angle (OZA) in order to partially account for differences between data points due to slant path [after *Nossal et al.*, 2001]. The OZA bins are defined as follows: OZA ≤ 15°, 15° < OZA ≤ 30°, 30° < OZA ≤ 45°.

[49] All observations were obtained >10 deg from the Galactic plan toward regions of low Galactic emission with | VLSR| ≥ 10 km/s.

8.1. Line Intensities

[50] Although intensity observations are not the central theme of this paper, line intensities are included to demonstrate the stability and reproducibility of the 2000–2001 data set. Balmer α intensities for all 1404 spectra, and 198 for a single new moon period (March, 2000) are plotted in Figure 4 as a function of LOS shadow altitude. See *Mierkiewicz et al.* [2006] for details regarding absolute intensity calibration and extinction corrections.

[51] Nighttime zenith Balmer α intensities ranged from ~15 R for low LOS shadow altitudes (i.e., observations near the terminator) to ~2 R at 20,000 km. As shadow altitude increases, less hydrogen is directly illuminated by solar Lyman β radiation and the emission intensity decreases. Eventually a plateau is reached (near 10,000 km shadow altitude in Figure 4) as contributions to Balmer α from the multiple scattering of Lyman β into the earth's shadow become a large fraction of the total observed emission [see, e.g., *Anderson et al.*, 1987].

[52] Morning intensities were, on average, typically ~20% brighter than evening intensities for similar LOS shadow altitudes, with the dusk to dawn intensity asymmetry most apparent at shadow altitudes ≤2000 km (see Figure 4). The magnitude of this dusk to dawn intensity asymmetry is consistent with earlier observations by *Tinsley* [1970] and others. Detailed radiative transport analysis is necessary, taking into account contributions due to multiple scattering and differences in viewing geometry, in order to interpret these observed intensity changes in terms of the magnitude of change in the underlying hydrogen distribution [see, e.g., *Bishop et al.*, 2004].

8.2. Cascade Contributions to the Line

[53] In order to retrieve the most accurate exospheric effective temperatures from Balmer α line profile observations, the line profile fitting procedure must account for cascade contributions to the line [*Nossal et al.*, 1997, 1998]. All spectra were fit with a two cluster Gaussian model taking into account direct solar Lyman β excitation and cascade contributions to the line. Based on spectra obtained from a restricted set of viewing geometries (see below), the 2000–2001 PBO data set indicates a cascade contribution at Balmer α of 5 ± 3%; refer to Figure 5.

Table 3. The 2000–2001 Balmer α Data Set: Nights 33–64

Night	Series	Date	Day[a]	Spc[b]	IP[c]	F10.7	Ap
33	9	11/03/00	308	11	5	196	03
34	9	11/04/00	309	11	3	191	26
35	10	11/22/00	327	24	4	190	08
36	10	11/24/00	329	15	5	192	11
37	10	12/03/00	338	26	5	159	10
38	11	01/18/01	18	22	4	147	04
39	11	01/20/01	20	44	6	148	09
40	11	01/21/01	21	44	4	147	19
41	11	01/22/01	22	30	5	157	12
42	11	01/25/01	25	35	7	163	06
43	12	02/17/01	48	17	4	127	02
44	12	02/18/01	49	30	7	129	03
45	12	02/21/01	52	40	7	141	06
46	12	03/01/01	60	15	4	129	06
47	13	03/27/01	86	9	3	272	27
48	13	03/28/01	87	29	6	272	44
49	14	04/27/01	117	3	0	193	04
50	15	05/19/01	139	36	4	145	10
51	16	07/14/01	195	5	0	*145	12
52	16	07/15/01	196	1	2	*147	10
53	17	08/14/01	226	14	2	151	10
54	17	08/20/01	232	43	5	160	06
55	17	08/21/01	233	45	7	164	13
56	18	09/25/01	268	27	3	277	33
57	18	09/27/01	270	24	3	271	11
58	19	10/17/01	290	37	6	216	04
59	19	10/18/01	291	2	1	227	03
60	19	10/19/01	292	2	1	246	09
61	20	11/12/01	316	18	8	223	02
62	20	11/17/01	321	18	4	194	13
63	20	11/20/01	324	13	4	181	08
64	20	11/21/01	325	13	4	180	04
Total				1404			

[a]Day number; year 2000 was a leap year, as such 02/29/00 is day 60.
[b]Number of spectra with: shadow altitudes <20,000 km, observation zenith distances ≤45°, galactic latitudes >10° from the plain (l = 0).
[c]Number of instrumental profiles (IPs) collected per night.

Table 4. The 2000–2001 New Moon Dates and Series Numbers for 20 New Moon Periods Where Observations Were Obtained From PBO

New Moon	Day	Series	F10.7	Ap	T[a] (K)	Spc[b]
01/06/00	06	1	140	19	697 ± 45	12
02/05/00	36	2	163	12	796 ± 54	52
03/06/00	66	3	219	12	899 ± 58	62
04/04/00	95	4	207	22	899 ± 77	44
05/04/00	125	5	137	6	943 ± 58	50
06/02/00	154	6	193	6	824 ± 44	44
07/01/00	183	–	–	–	–	–
07/31/00	213	–	–	–	–	–
08/29/00	242	7	166	35	852 ± 52	43
09/27/00	271	8	205	11	988 ± 70	11
10/27/00	301	9	174	4	923 ± 97	16
11/25/00	330	10	197	6	817 ± 71	31
12/25/00	360	–	–	–	–	–
01/24/01	24	11	167	20	722 ± 121	79
02/23/01	54	12	142	10	816 ± 96	42
03/25/01	84	13	216	6	900 ± 94	21
04/23/01	113	14	199	16	994 ± 40	3
05/23/01	143	15	163	9	843 ± 103	36
06/21/01	172	–	–	–	–	–
07/20/01	201	16	147	4	712 ± 41	6
08/19/01	231	17	161	8	718 ± 80	97
09/17/01	260	18	201	6	839 ± 56	20
10/16/01	289	19	206	7	849 ± 74	13
11/15/01	319	20	202	9	826 ± 90	17
12/14/01	348	–	–	–	–	–

[a]Effective temperature computed for observations where LOS shadow altitude ≥200 km and LOS shadow altitude <1500 km.
[b]200 km ≤ number of spectra <1500 km.

[54] Cascade contributions were determined from observations at least 60 degrees from the Galactic plane, with a significant Doppler shift in the Galactic emission away from the red-wing of the Balmer α emission line (i.e., VLSR < −10 km/s or VLSR > +35). Only 17% of the 1404 spectra in this data set met these restrictions. These cuts helped ensure that small amounts of Galactic emission (i.e., at the sub Rayleigh level) were not mistakenly fit as cascade contributions to the geocoronal emission line. Furthermore, the improved optical system of the PBO Fabry-Perot, with its 75 km/s spectral baseline centered on Balmer α, combined with fixed pressure operation and observations made while tracking at the sidereal rate, allowed better identification and characterization of Galactic background emission [*Mierkiewicz et al.*, 2006].

8.3. Exospheric Effective Temperatures

[55] Balmer α effective temperatures for all 1404 spectra are plotted in Figure 6 as a function of LOS shadow altitude.

[56] A predominate feature in Figure 6 is the distinctive decrease in exospheric effective temperature with increasing altitude. Applying a linear fit to the combined pm + am data set (Figure 6, solid line), the slope is found to be −20 K per 1000 km, representing a ∼470 K decrease in effective temperature over the shadow altitude range sampled, from ∼840 K near 500 km altitude to ∼370 K near 20,000 km.

[57] The average effective temperature for all 152 observations (pm + am combined) falling between 400 km and 600 km LOS shadow altitude (i.e., near the nominal exobase) was 830 K.

[58] One hundred and fifty-two spectra were used to determine the 830 K near-exobase effective temperature, of which 78 were obtained near the evening exobase and 74 near the morning exobase. When parsed into dusk and dawn observations, no statistically significant evening/morning variation in the exobase effective temperature is detected.

8.4. Seasonal Variations in the Near-Exobase Effective Temperature

[59] Effective temperatures for series 1–10 (2000) and 11–20 (2001) are plotted as a function of LOS shadow altitude in Figures 7 and 8. A decrease in exospheric effective temperature with increasing LOS shadow altitude is a persistent feature in every night of PBO observations in which a wide range of shadow altitudes were observed.

[60] The observed Balmer α column emission is a convolution of emissions from many different populations of hydrogen atoms (i.e., ballistic, escape, satellite), in some cases from all over the globe due to the long mean free paths of exospheric particles. At low LOS shadow altitudes (i.e., near the nominal exobase), however, the profile is more likely to be dominated by contributions from ballistic atoms originating in the thermosphere and therefore more representative of a kinetic temperature [*Bishop and Chamberlain*, 1987].

[61] We have explored line profile variations where the kinetic temperature is most likely to be the dominate line profile signature by limiting observations to those below an upper limit LOS shadow altitude. In this study a LOS shadow altitude cutoff of 1500 km was used, limiting observations to within 1000 km of the nominal exobase (∼500 km). Evening and morning (pm + am) observations were combined in order to ensure complete seasonal coverage, obtaining the largest sample of data within the bounds of LOS shadow altitude limit. A reproducible semiannual near-exobase effective temperature variation was detected with maxima near day numbers 100 and 300 and minima near day numbers 1 and 200, ranging from ∼710 to 975 K. Refer to Figure 9. Average near-exobase effective temperatures, corresponding series numbers, and new moon dates are listed in Table 4. The uncertainties shown in Figure 9 (and quoted in Table 4) are the standard deviation of the range of temperatures observed during each dark moon observing window. In most cases this value is larger than the instrumental uncertainty which is estimated to be about ±40 K at 800 K.

9. Conclusions and Discussion

[62] The data presented in this paper are the first geocoronal line profile observations obtained with a Fabry-Perot spectrometer employing an optical system specifically designed for the annular summing technique [*Mierkiewicz et al.*, 2006]. The net result is an instrument capable of making geocoronal observations with signal-to-noise ratios of ∼100 in 10 min, covering a nearly unvignetted 75 km/s spectral interval with 3.75 km/s velocity resolution. The achieved high signal-to-nose ratios were critical to exploring profile perturbations at the few percent level, as was the extended spectral baseline which helped us to identify and avoid sub-Rayleigh Galactic Balmer α contamination.

[63] This second generation Fabry-Perot annular summing spectrometer enabled the acquisition of a comprehensive monthly data set spanning 20 dark moon periods during

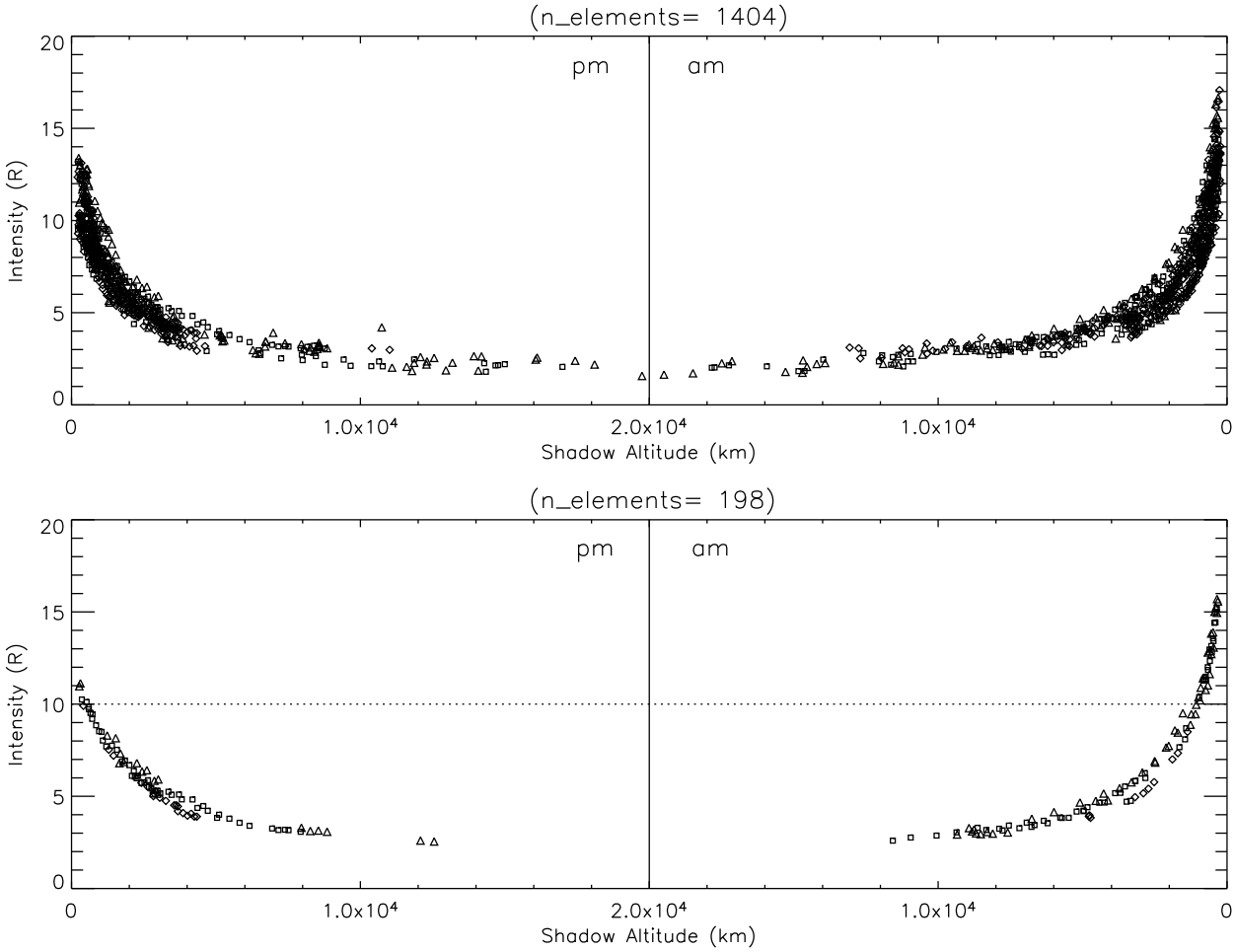

Figure 4. (top) Balmer α intensities for the entire 2000–2001 PBO data set (1404 spectra) as a function of LOS shadow altitude (km) separated into pre- and post-midnight sets. Low shadow altitude intensities for the morning exosphere are typically 20% brighter than evening intensities for the same viewing geometry. (bottom) A subset of the intensity observations obtained during observation series 3 (March, 2000). Plotting symbols: diamonds correspond to OZA $\leq 15°$, squares correspond to $15° <$ OZA $\leq 30°$, and triangles correspond to $30° <$ OZA $\leq 45°$.

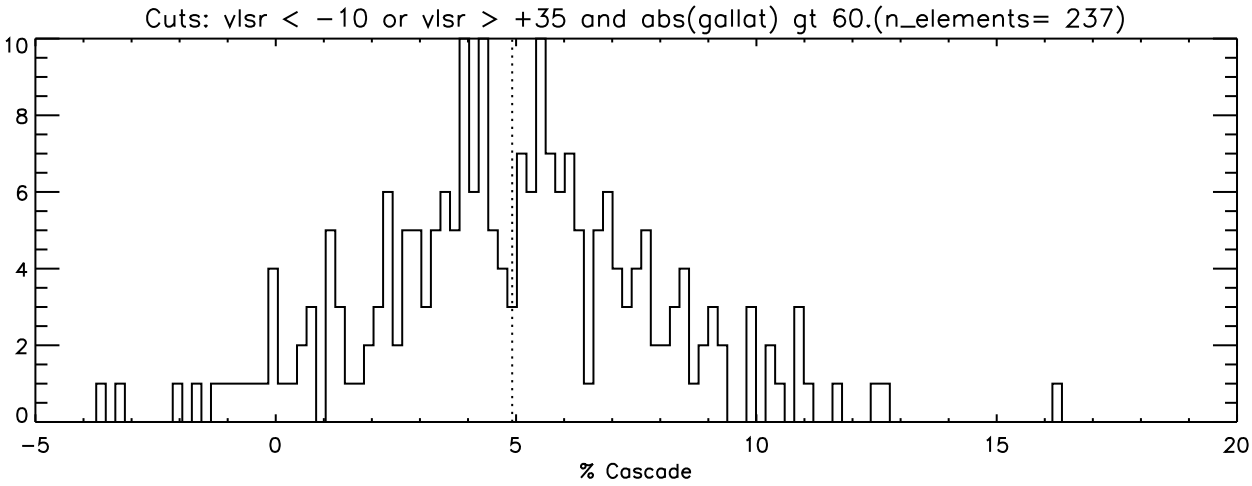

Figure 5. Histogram of % cascade contribution to the line. The vertical dotted line indicates the average value of $5 \pm 3\%$ (where the uncertainty is based on the spread of the distribution). Two limits were used to restrict the cascade data set: VLSR < -10 km/s or VLSR > 35 km/s and a pointing direction at least 60 degrees from the Galactic plane.

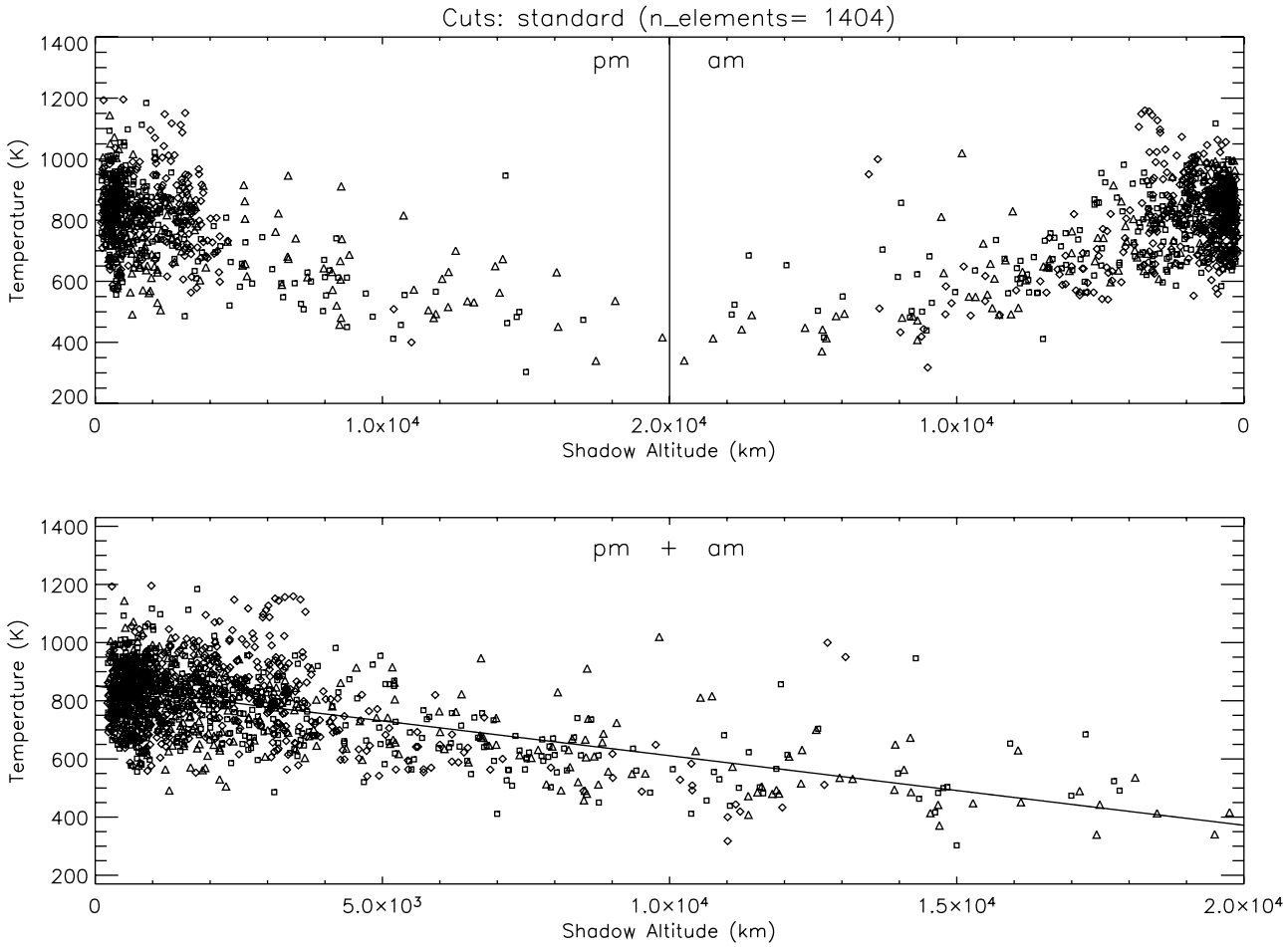

Figure 6. Balmer α Doppler widths for the entire 2000–2001 PBO data set (1404 spectra) as a function of LOS shadow altitude (km). (top) Doppler width data separated into pre- and post-midnight sets. (bottom) Evening and morning Doppler width data combined. A persistent narrowing of the profile with shadow altitude is apparent in the majority of the PBO data; a decrease of ~470 K in terms of effective temperature from ~840 K near 500 km to ~370 K near 20,000 km. Solid line is a linear fit to the data. Plotting symbols: diamonds correspond to OZA $\leq 15°$, squares correspond to $15° <$ OZA $\leq 30°$, and triangles correspond to $30° <$ OZA $\leq 45°$.

2000–2001. Based on our analysis of the observed Balmer α column emissions, we report the detection of a reproducible semiannual variation in the near-exobase effective temperature, with maxima near day numbers 100 and 300 and minima near day numbers 1 and 200.

9.1. Cascade

[64] We have determined a cascade contribution at Balmer α of 5 $\pm$ 3% of the total intensity, consistent with the work of R. R. Meier (private communication, 2000) (see section 3).

[65] *Nossal et al.* [1998] detected a ~10% cascade contribution in their CCD demonstration observations. At the time, this value appeared to be consistent with, although slightly higher than, the 7% contribution predicted by *Meier* [1995]. Since 1998, revised calculations by R. R. Meier (private communication, 2000) reduced the predicted cascade contribution to ~4%.

[66] Although care was taken in the CCD demonstration observations by *Nossal et al.* [1998] to avoid regions of significant Galactic Balmer α emission, instrumental vignetting limited their spectral baseline, and it is likely that small amounts of Galactic contamination went unnoticed. The extended spectral baseline of the second generation annular summing spectrometer used in this new study allowed for a better characterization of the background, including Galactic contamination; this is especially important because the Galactic emission is ubiquitous and the

Figure 7. Year 2000 effective temperatures by series number (01–10). The diagonal dotted line is the linear fit obtained in the fit of the 1404 spectra pm + am combined data set (Figure 6). Shaded regions highlight observations taken below LOS shadow altitudes of 1500 km (the average of which is used in Figure 9). Plotting symbols: diamonds correspond to OZA $\leq 15°$, squares correspond to $15° <$ OZA $\leq 30°$, and triangles correspond to $30° <$ OZA $\leq 45°$.

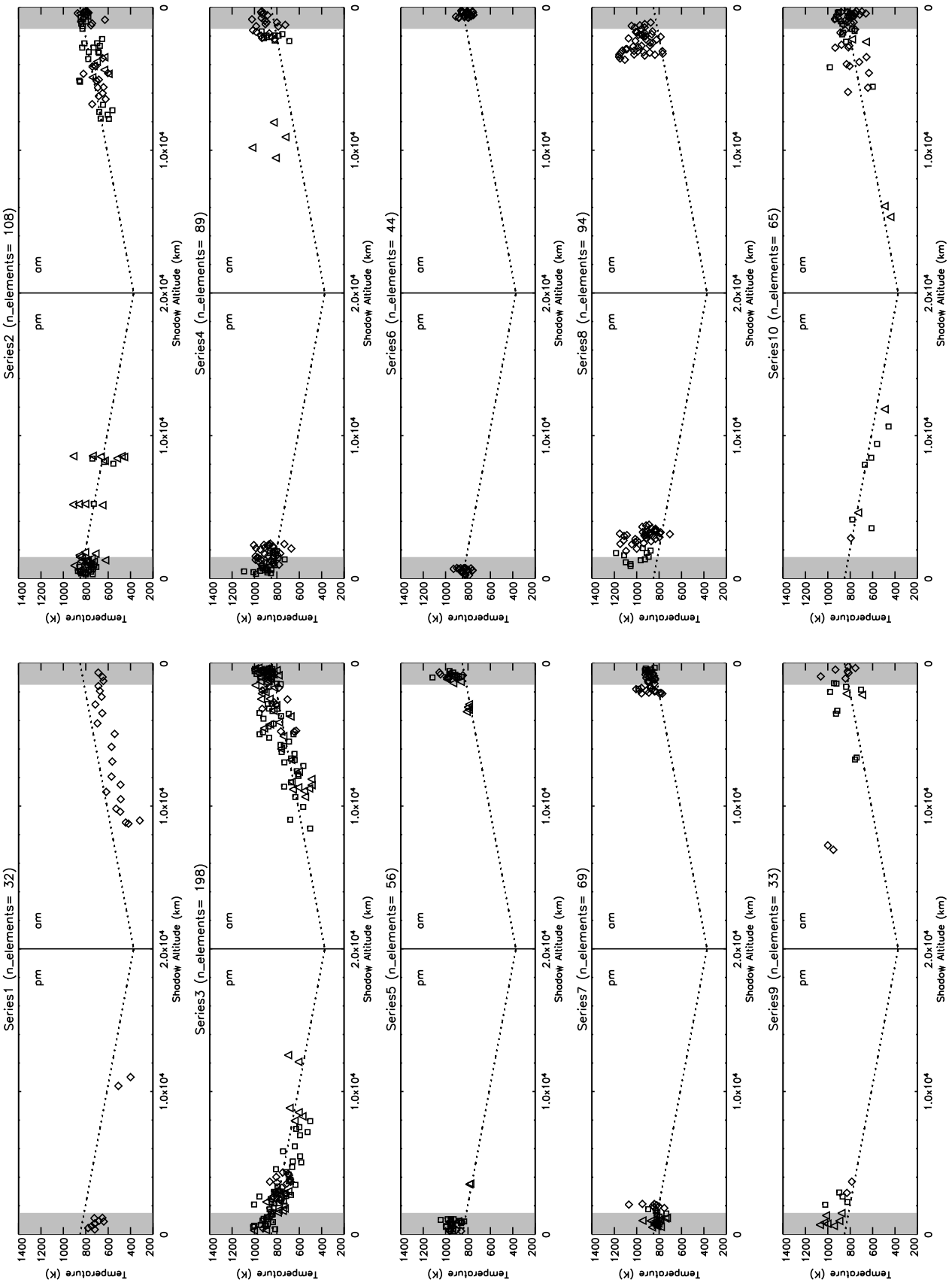
Series1 (n_elements= 32)
Series2 (n_elements= 108)
Series3 (n_elements= 198)
Series4 (n_elements= 89)
Series5 (n_elements= 56)
Series6 (n_elements= 44)
Series7 (n_elements= 69)
Series8 (n_elements= 94)
Series9 (n_elements= 33)
Series10 (n_elements= 65)
pm
am
Temperature (K)
Shadow Altitude (km)
0
2.0x10⁴
1.0x10⁴
200
400
600
800
1000
1200
1400

Figure 7

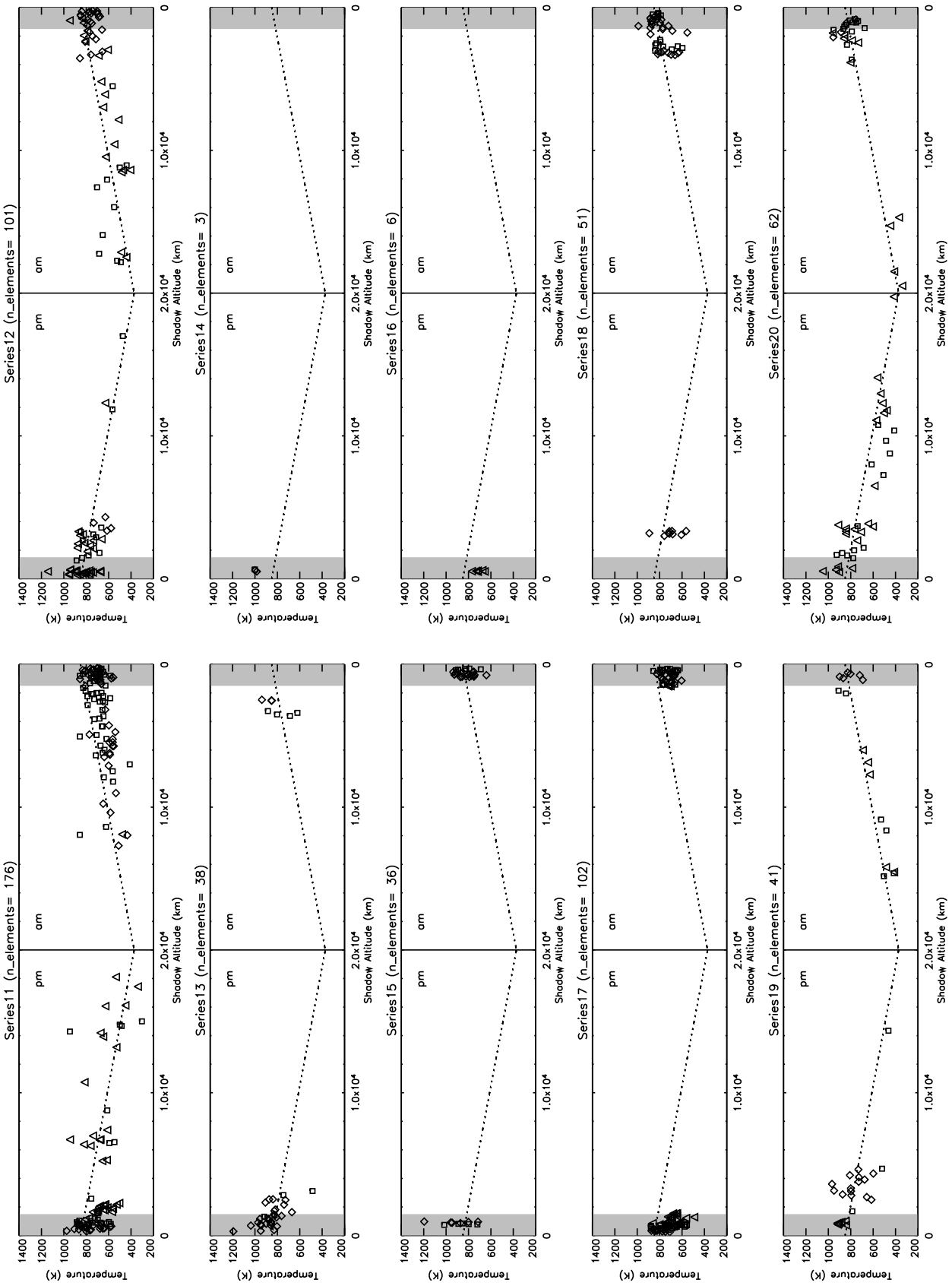
Series11 (n_elements= 176)
Series12 (n_elements= 101)
Series13 (n_elements= 38)
Series14 (n_elements= 3)
Series15 (n_elements= 36)
Series16 (n_elements= 6)
Series17 (n_elements= 102)
Series18 (n_elements= 51)
Series19 (n_elements= 41)
Series20 (n_elements= 62)
pm
am
Temperature (K)
Shadow Altitude (km)
0
1.0x10⁴
2.0x10⁴
200
400
600
800
1000
1200
1400

Figure 8

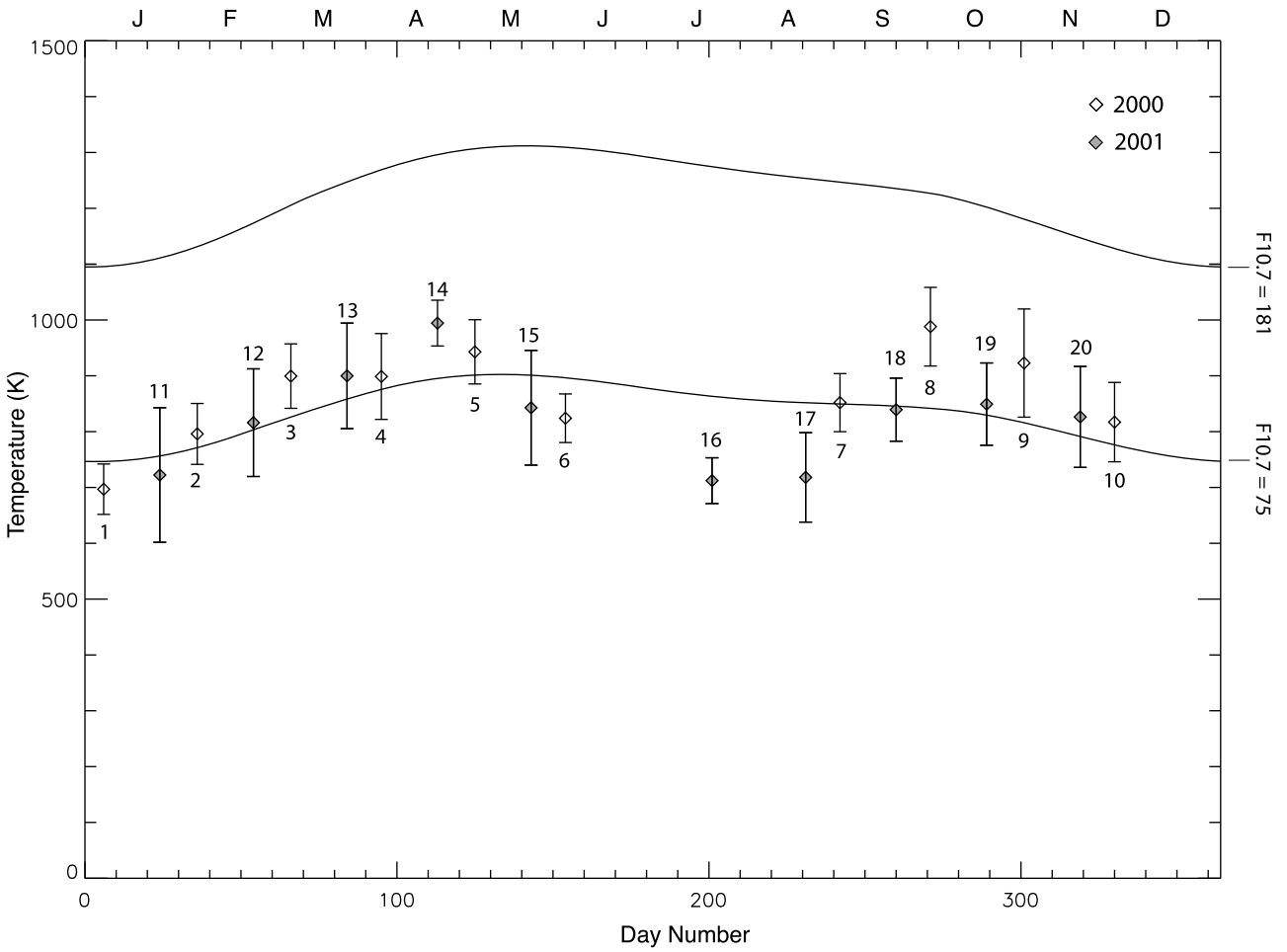

Figure 9. Exospheric effective temperatures derived from PBO line width observations obtained for shadow altitudes below 1500 km. Observations from each series were averaged and plotted on the new moon day number. Year 2000 observations are indicated by the open diamonds, 2001 observations by the filled symbols. Solid lines correspond to daily MSIS [*Hedin*, 1991] exobase temperatures (computed as discussed in section 8.3), run with daily and average F10.7 flux inputs set to 181 (corresponding to the 2000–2001 F10.7 average) and 75; all magnetic activity parameters (Ap indices) were set to 14. A semi-annual variation is observed in the column averaged exospheric effective temperature with maxima near day numbers 100 and 300 and minima near day numbers 1 and 200.

emission line is rather broad (~20 km/s *fwhm*). This extended baseline led to our requirement of a VLSR shift of <-10 km/s or $>+35$ for cascade studies; see *Mierkiewicz* [2002] and *Mierkiewicz et al.* [2006] for further details.

[67] Note, the observations presented here, and those of *Nossal et al.* [1998], were all collected near solar maximum; *Meier*'s [1995] and more recent cascade calculations are based on solar observations conducted near solar minimum.

9.2. Exospheric Effective Temperatures

[68] We have observed a decrease in effective temperature with increasing LOS shadow altitude for every night in which a wide range of shadow altitudes were sampled. This decrease is consistent with observations first made by *Meriwether et al.* [1980] and later by *Yelle and Roesler* [1985] and *Kerr et al.* [1986]. The CCD demonstration observations of *Nossal et al.* [1997] display smaller decreases in temperature with altitude, although it should be noted that altitude coverage was limited.

[69] Assuming a linear decrease in effective temperature with LOS shadow altitude (see Figure 6), our empirically determined -20 K per 1000 km gradient in effective temperature is in agreement with the early theoretical work of *Hartle* [1973].

[70] The significant line profile perturbations reported by *Kerr et al.* [1986] or the Lorentzian-like profiles observed at

Figure 8. Year 2001 effective temperatures by series number (11–20). The diagonal dotted line is the linear fit obtained in the fit of the 1404 spectra pm + am combined data set (Figure 6). Shaded regions highlight observations taken below LOS shadow altitudes of 1500 km (the average of which is used in Figure 9). Plotting symbols: diamonds correspond to OZA $\leq 15°$, squares correspond to $15° <$ OZA $\leq 30°$, and triangles correspond to $30° <$ OZA $\leq 45°$.)

very high shadow altitudes by *Yelle and Roesler* [1985] were not detected in our observations.

[71] The average exobase temperature computed from the Mass Spectrometer Incoherent Scatter (MSIS) model of *Hedin* [1991] for the 2000–2001 period was 1217 K, ~1.5× higher than the observed two-year PBO average effective temperature of 830 K for observations obtained with the base of the observed column emission (i.e., the LOS shadow altitude) near the nominal exobase. The MSIS temperature was computed by running MSIS for each day of the year at one minute intervals per day (corresponding to 1,440 steps per day) for PBO's latitude and longitude. Daily and average F10.7 cm flux inputs were set to 181, all magnetic activity parameters (Ap indices) were set to 14; these values correspond to 2000–2001 average solar/geophysical conditions. Finally, the 1217 K MSIS exobase temperature was derived by taking the yearly average of the daily average of the exobase maximum and minimum temperatures, $(T_{max} + T_{min})/2$.

[72] As shown in Figure 9, we have detected a reproducible semiannual variation in near-exobase effective temperatures with maxima near day numbers 100 and 300 and minima near day numbers 1 and 200. Temperatures ranged from ~710 to 975 K. The solid lines in Figure 9 are daily MSIS exobase temperatures computed as discussed above, with daily and average F10.7 cm flux inputs set to 181 (upper line, corresponding to the two-year 2000–2001 F10.7 average) and 75 (lower line); all magnetic activity parameters (Ap indices) were set to 14. The F10.7 cm flux input of 75 (lower line in Figure 9) was selected to scale the MSIS model derived temperatures to the range of the PBO observations, a further indication that our observations are consistently lower than those predicted by the MSIS model. A semiannual temperature variation is apparent in both MSIS runs, but the magnitude of this variation is less than that of our observations.

[73] *Anderson et al.* [1987] presented a comprehensive study of Lyman β transport in the upper atmosphere based on three hydrogen density distributions (solar minimum, medium and maximum) constructed from Monte Carlo simulations of *Tinsley et al.* [1986]. The *Anderson et al.* [1987] study provides predictions for geocoronal Balmer α intensities and temperatures for a variety of look directions for each of the three cases of solar activity; predictions are for a latitude of 24°. Of particular interest here are the *Anderson et al.* [1987] line profile results for zenith viewing directions at solar depression angles (SDAs) of 20° and 80° for mean spherically symmetric density and temperature models corresponding to solar minimum and maximum conditions.

[74] Calculating contributions to the Balmer α column emission for solar minimum and maximum, *Anderson et al.* [1987] show that a larger fraction of the observed column emission originates from higher, cooler regions of the exosphere at solar maximum than minimum, and that the observed effective temperature at solar maximum for zenith viewing will actually be *lower* than that at solar minimum (in spite of the higher exobase temperatures at solar maximum).

[75] *Anderson et al.* [1987] compared line profile model results with the ground-based observations of *Meriwether et al.* [1980] and *Yelle and Roesler* [1985], finding good model agreement with the low temperatures observed at high SDAs (i.e., shadow altitudes). At small SDAs, the temperatures of *Meriwether et al.* [1980] and *Yelle and Roesler* [1985] were higher than that predicted by the model.

[76] The *Anderson et al.* [1987] study also indicates that very little evening/morning variation in the exobase temperature will be observed at solar maximum, with morning observations expected only to be ~20 K cooler than evening observations for zenith observations at solar maximum. This result is consistent with our lack of detection of an observed evening/morning temperature variation in the derived effective temperature at LOS shadow altitudes near the nominal exobase.

[77] Based on the *Anderson et al.* [1987] study, it seems likely that the approximately 1.5× offset between our Balmer α line width derived effective temperatures and the MSIS model may be explained by contributions to the observed Balmer α column emission from higher, cooler regions of the exosphere as well as some contribution from multiple scattering into the cooler lower regions of the thermosphere below. Detailed radiative transport modeling, incorporating realistic hydrogen density and velocity distributions will be needed to sort this out.

[78] Although the interpretation of the Balmer α profile in terms of an effective temperature may result in masking important physical signatures in the profile itself (e.g., evidence for escape and other non-Gaussian signatures), we have shown that effective temperatures derived from Balmer α column emission observations are a useful metric to track variability in the exosphere with altitude and season. We also find that for shadow altitudes below our limit of 20,000 km, and in directions that carefully minimize Galactic background contamination, fits with Gaussian profiles that take into account all fine structure paths known to be present in direct and cascade emission show no evidence for non-Gaussian line profile signatures, as indicated by the lack of significant residuals in the fits (see, e.g., Figure 2).

[79] **Acknowledgments.** The authors would like to thank R. C. Woodward for his help implementing the Voigt-fit code. Shadow altitude and VLSR calculations were determined by an algorithm provided by J. Percival of the University of Wisconsin's Space Astronomy Lab. Our observations rely heavily on engineering support by K. Jaehnig. This work was supported by the NSF through award AGS-0940270.

[80] Robert Lysak thanks the reviewers for their assistance in evaluating this paper.

References

Anderson, D. E., Jr., R. R. Meier, R. R. Hodges, and B. A. Tinsley (1987), Hydrogen Balmer alpha intensity distributions and line profiles from multiple scattering theory using realistic geocoronal models, *J. Geophys. Res.*, *92*, 7619–7642, doi:10.1029/JA092iA07p07619.

Atreya, S. K., P. B. Hays, and A. F. Nagy (1975), Doppler profile measurements of the geocoronal hydrogen Balmer alpha line, *J. Geophys. Res.*, *80*, 635–638, doi:10.1029/JA080i004p00635.

Bertaux, J. L. (1978), Interpretation of OGO-5 line shape measurements of Lyman-alpha emission from terrestrial exospheric hydrogen, *Planet. Space Sci.*, *26*, 431–447, doi:10.1016/0032-0633(78)90065-X.

Bertaux, J. L., and J. E. Blamont (1970), OGO-5 measurements of Lyman-alpha intensity distribution and linewidth up to 6 earth radii, *Space Res.*, *10*, 591–601.

Bethe, H. A., and E. E. Salpeter (1957), *Quantum Mechanics of One- and Two-Electron Atoms*, Academic, San Diego, Calif.

Bishop, J., and J. W. Chamberlain (1987), Geocoronal structure: 3. Optically thin, Doppler-broadened line profiles, *J. Geophys. Res.*, *92*(A11), 12,389–12,397, doi:10.1029/JA092iA11p12389.

Bishop, J., J. Harlander, S. M. Nossal, and F. L. Roesler (2001), Analysis of Balmer α intensity measurements near solar minimum, *J. Atmos. Sol. Terr. Phys.*, *63*(4), 341–353, doi:10.1016/S1364-6826(00)00212-1.

Bishop, J., E. J. Mierkiewicz, F. L. Roesler, J. F. Gómez, and C. Morales (2004), Data-model comparison search analysis of coincident PBO Balmer α, EURD Lyman β geocoronal measurements from March 2000, *J. Geophys. Res.*, *109*, A05307, doi:10.1029/2003JA010165.

Chamberlain, J. W. (1963), Planetary coronae and atmospheric evaporation, *Planet. Space Sci.*, *11*, 901–960, doi:10.1016/0032-0633(63)90122-3.

Chamberlain, J. W. (1976), Spectral line profiles for a planetary corona, *J. Geophys. Res.*, *81*, 1774–1776, doi:10.1029/JA081i010p01774.

Chamberlain, J. W. (1987), Balmer profiles in the geocorona and interstellar space. I—Asymmetries due to fine structure, *Icarus*, *70*, 476–482, doi:10.1016/0019-1035(87)90089-3.

Coakley, M. M., F. L. Roesler, R. J. Reynolds, and S. M. Nossal (1996), Fabry Perot CCD annular-summing spectroscopy: Study and implementation for aeronomy applications, *Appl. Opt.*, *35*(33), 6479–6493, doi:10.1364/AO.35.006479.

Daehler, M., and F. L. Roesler (1968), High contrast in a polyetalon Fabry-Perot spectrometer, *Appl. Opt.*, *7*(6), 1240–1241, doi:10.1364/AO.7.001240.

Garcia, J. D., and J. E. Mack (1965), Energy level and line tables for one-electron atomic spectra, *J. Opt. Soc. Am.*, *55*(6), 654–661.

Hartle, R. E. (1973), Density and temperature distributions in non-uniform rotating planetary exospheres with applications to earth, *Planet. Space Sci.*, *21*, 2123–2137.

Hays, P. B., and R. G. Roble (1971), A technique for recovering Doppler line profiles from Fabry-Perot interferometer fringes of very low intensity, *Appl. Opt.*, *10*, 193–200, doi:10.1364/AO.10.000193.

Hinteregger, H. E., K. Fukui, and B. R. Gilson (1981), Observational, reference and model data on solar EUV, from measurements on AE-E, *Geophys. Res. Lett.*, *8*, 1147–1150, doi:10.1029/GL008i011p01147.

Haffner, L. M. (1999), The warm ionized medium: Distribution, kinematics, and physical conditions, PhD thesis, 134 pp., Univ. of Wisc.-Madison, Madison.

Haffner, L. M., R. J. Reynolds, S. L. Tufte, G. J. Madsen, K. P. Jaehnig, and J. W. Percival (2003), The Wisconsin H-Alpha Mapper Northern Sky Survey, *Astrophys. J. Suppl. Ser.*, *149*(2), 405–422, doi:10.1086/378850.

He, X., R. B. Kerr, J. Bishop, and C. A. Tepley (1993), Determining exospheric hydrogen density by reconciliation of H-alpha measurements with radiative transfer theory, *J. Geophys. Res.*, *98*(A12), 21,611–21,626, doi:10.1029/93JA01854.

Hedin, A. E. (1991), Extension of the MISIS thermosphere model into the middle and lower atmosphere, *J. Geophys. Res.*, *96*, 1159–1172, doi:10.1029/90JA02125.

Jacchia, L. G. (1971), Revised static models of the thermosphere and exosphere with empirical temperature profiles, *SAO Spec. Rep. 332*, Smithson. Astrophys. Observ., Cambridge, Mass.

Kerr, R. B., and J. H. Hecht (1996), Measurement of geocoronal Balmer alpha in the auroral zone, *J. Geophys. Res.*, *101*(A1), 189–194, doi:10.1029/95JA01818.

Kerr, R. B., and C. A. Tepley (1988), Ground-based measurements of exospheric hydrogen density, *Geophys. Res. Lett.*, *15*, 1329–1332, doi:10.1029/GL015i012p01329.

Kerr, R. B., S. K. Atreya, J. W. Meriwether, C. A. Tepley, and R. G. Burnside (1986), Simultaneous H-alpha line profile and radar measurements at Arecibo, *J. Geophys. Res.*, *91*, 4491–4512, doi:10.1029/JA091iA04p04491.

Kerr, R. B., et al. (2001a), Secular variability of the geocoronal Balmer-alpha brightness: Magnetic activity and possible human influences, *J. Geophys. Res.*, *106*(A12), 28,819–28,830, doi:10.1029/1999JA900187.

Kerr, R. B., et al. (2001b), Periodic variations of geocoronal Balmer-alpha brightness due to solar-driven exospheric abundance variations, *J. Geophys. Res.*, *106*(A12), 28,797–28,818, doi:10.1029/1999JA900186.

Meier, R. R. (1995), Solar Lyman series line profiles and atomic hydrogen excitation rates, *Astrophys. J.*, *452*, 462–471, doi:10.1086/176318.

Meriwether, J. W., Jr., S. K. Atreya, T. M. Donahue, and R. G. Burnside (1980), Measurements of the spectral profile of Balmer Alpha emission from the hydrogen geocorona, *Geophys. Res. Lett.*, *7*, 967–970, doi:10.1029/GL007i011p00967.

Mierkiewicz, E. J. (2002), Fabry-Perot observations of the hydrogen geocorona, PhD thesis, Univ. of Wisc.-Madison, Madison.

Mierkiewicz, E. J., F. L. Roesler, S. M. Nossal, and R. J. Reynolds (2006), Geocoronal hydrogen studies using Fabry Perot interferometers, part 1: Instrumentation, observations, and analysis, *J. Atmos. Sol. Terr. Phys.*, *68*(13), 1520–1552, doi:10.1016/j.jastp.2005.08.024.

Nossal, S., R. J. Reynolds, F. L. Roesler, F. Scherb, and J. Harlander (1993), Solar cycle variations of geocoronal Balmer alpha emission, *J. Geophys. Res.*, *98*(A3), 3669–3676, doi:10.1029/92JA02568.

Nossal, S., F. L. Roesler, M. M. Coakley, and R. J. Reynolds (1997), Geocoronal hydrogen Balmer α line profiles obtained using Fabry-Perot annular summing spectroscopy: Effective temperature results, *J. Geophys. Res.*, *102*(A7), 14,541–14,554, doi:10.1029/97JA00293.

Nossal, S., F. L. Roesler, and M. M. Coakley (1998), Cascade excitation in the geocoronal hydrogen Balmer α line, *J. Geophys. Res.*, *103*(A1), 381–390, doi:10.1029/97JA02435.

Nossal, S. M., F. L. Roesler, J. Bishop, R. J. Reynolds, L. M. Haffner, S. Tufte, J. Percival, and E. J. Mierkiewicz (2001), Geocoronal Hα intensity measurements using the Wisconsin Hα Mapper Fabry-Perot facility, *J. Geophys. Res.*, *106*(A4), 5605–5616, doi:10.1029/2000JA000003.

Nossal, S. M., F. L. Roesler, E. J. Mierkiewicz, R. J. Reynolds (2004), Observations of solar cyclical variations in geocoronal Hα column emission intensities, *Geophys. Res. Lett.*, *31*, L06110, doi:10.1029/2003GL018729.

Nossal, S. M., E. J. Mierkiewicz, F. L. Roesler, L. M. Haffner, R. J. Reynolds, and R. C. Woodward (2008), Geocoronal hydrogen observations spanning three solar minima, *J. Geophys. Res.*, *113*, A11307, doi:10.1029/2008JA013380.

Reynolds, R. J., F. Scherb, and F. L. Roesler (1973), Observations of diffuse galactic Hα and [N II] emission, *Astrophys. J.*, *185*, 869–876, doi:10.1086/152461.

Roesler, F. L. (1974), Fabry-Perot instruments of astronomy, in *Methods of Experimental Physics*, vol. 12A, *Astrophysics, Part A: Optical and Infrared*, pp. 531–569, Academic, New York.

Shih, P., F. L. Roesler, and F. Scherb (1985), Intensity variations of geocoronal Balmer alpha emission: 1. Observational results, *J. Geophys. Res.*, *90*, 477–490, doi:10.1029/JA090iA01p00477.

Tinsley, B. A. (1970), Variations of Balmer alpha emission and related hydrogen distributions, *Space Res.*, *10*, 582–590.

Tinsley, B. A., R. R. Hodges Jr., and R. P. Rohrbaugh (1986), Monte Carlo models for the terrestrial exosphere over a solar cycle, *J. Geophys. Res.*, *91*, 13,631–13,647, doi:10.1029/JA091iA12p13631.

Tousey, R., W. E. Austin, J. D. Purcell, and K. G. Widing (1965), The extreme ultraviolet emission from the Sun between the Lyman-alpha lines of H I and C VI, *Ann. Astrophys.*, *28*, 755–773.

Vernazza, J. E., and E. M. Reeves (1978), Extreme ultraviolet composite spectra of representative solar features, *Astrophys. J. Suppl. Ser.*, *37*, 485–513, doi:10.1086/190539.

Warren, H. P., J. T. Mariska, and K. Wilhelm (1998), High-resolution observations of the solar hydrogen Lyman lines in the quiet Sun with the SUMER instrument on SOHO, *Astrophys. J. Suppl. Ser.*, *119*(1), 105–120, doi:10.1086/313151.

Yelle, R. V., and F. L. Roesler (1985), Geocoronal Balmer alpha line profiles and implications for the exosphere, *J. Geophys. Res.*, *90*, 7568–7580, doi:10.1029/JA090iA08p07568.